

# Cuspidal Attractor in Slender Films Self-Organized By Thermocapillary Shear

Chengzhe Zhou and Sandra M. Troian\*

*California Institute of Technology, 1200 E.*

*California Blvd., MC 128-95, Pasadena, CA 91125*

(Dated: February 9, 2018)

## Abstract

Thermocapillary forces in slender films can trigger an instability resembling lenslet arrays. Here we predict subsequent evolution of stable yet dynamic conical shapes by a self-reinforcement mechanism that drives the liquid tip toward a virtual cusp singularity. While cusps are known to form in systems governed by normal forces, this work reveals how a surface shear singularity acts to self-organize fluid into a self-similar conical form. The evolution process suggests a novel method for non-contact fabrication of conical microarrays for micro-optical, superhydrophobic or biomimetic applications.

Astonishing singularities resembling line and point cusps are known to form in liquid systems. A recent delightful book by J. Eggers [1] (and many pertinent references therein) describes the complex dynamics of cusp formation leading to the breakup of a liquid thread, the Rayleigh–Taylor instability in Hele–Shaw cells and slender films undergoing rupture as sketched in Fig. 1(a) and (b) where a repulsive van der Waals force cause dewetting [2, 3]. Bernoff, Bertozzi and Witelski [4] have provided an elegant comprehensive framework for analyzing such singularities in slender shear-free films. Inspired by their work, we report here how similar cusps are also possible in films exposed to an applied surface shear. Fig.1 (c) and (d) depicts how a liquid film self-organizes into a dynamic cuspidal shape in response to large thermocapillary forces. (While cusps have been examined in one other system subject to surface shear [5, 6], the formation process was not addressed and remains an unsolved problem.)

Microarrays consisting of solid conical structures would make possible truly unique substrates for applications ranging from micro-optical beam shaping to biomimetic design of superhydrophobic, self-cleaning surfaces mimicking a cicada’s wing, as shown in Fig. 2. This concept can become a reality by exploiting recent advances in one-step, non-contact fabrication of 3D protrusion arrays triggered by electrohydrodynamic [8] or thermocapillary instabilities [9]. Here we examine for the first time the intermediate dynamics of the latter case in which initially rounded lenslets transform into stable, conical shapes by a self-reinforcement mechanism that drives the tip shape toward a virtual cusp singularity. The

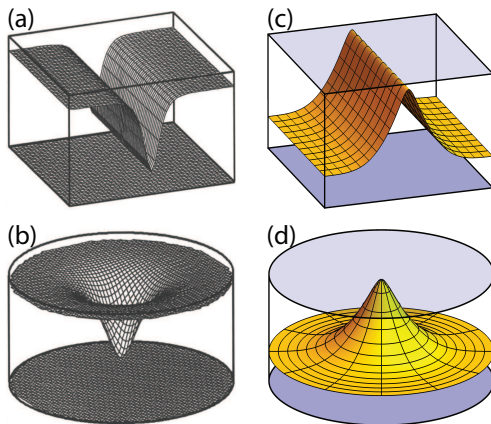


FIG. 1. (Color online) (a) Line and (b) point rupture of a thin dewetting film. (Courtesy Ref. [7]). (c) Line and (d) point cusp formation in response to large thermocapillary forces.

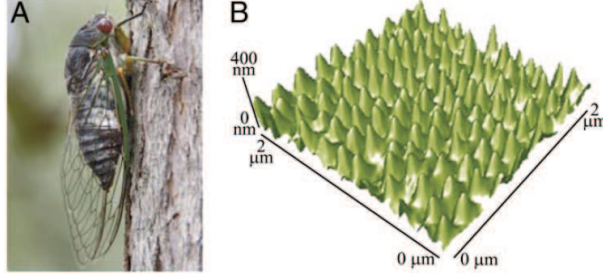


FIG. 2. (Color online) (a) Resting cicada. (b) AFM image of a superhydrophobic, self-cleaning conical array on a cicada wing. Courtesy Ref. [10].

relevant geometry is sketched in Fig. 3 where two parallel substrates held at a constant temperature difference  $\Delta T = T_{\text{hot}} - T_{\text{cold}} > 0$  and in close proximity ( $d$  is typically a few microns or less) confine a slender fluid bilayer (air and liquid). The ratio  $(h_o/\lambda_{\text{max}})^2 \ll 1$ ) such that the thermal flux is dominated by vertical conduction where  $\lambda_{\text{max}}$  is the wavelength of the fastest growing, linearly unstable mode [11, 12]. Fluctuations along the free surface experience large thermocapillary stresses due to the small ratio of air to liquid thermal conductivity  $0 < \kappa < 1$ . The non-dimensional evolution equation is

$$\frac{\partial \hat{H}}{\partial \hat{T}} + \nabla_{\parallel} \cdot \left\{ \frac{\hat{H}^3}{3\overline{Ca}} \nabla_{\parallel}^3 \hat{H} + \frac{\kappa \hat{D} \overline{Ma} \hat{H}^2}{2[\hat{D} + (\kappa - 1)\hat{H}]^2} \nabla_{\parallel} \hat{H} \right\} = 0 \quad (1)$$

where  $\nabla_{\parallel}$  denotes the in-plane gradient operator. Vertical dimensions are scaled by  $h_o$  and lateral ones by  $\lambda_{\text{max}}$  such that  $\hat{Z} = z/h_o$ ,  $\hat{H} = h(\mathbf{x}, t)/h_o$ ,  $\hat{D} = d_o/h_o$  and  $\hat{\mathbf{X}} = \mathbf{x}/\lambda_{\text{max}}$ . Time is likewise normalized as  $\hat{T} = u_c t/\lambda_{\text{max}}$  where  $u_c$  is a characteristic thermocapillary flow speed. These scalings give rise to two dimensionless numbers  $\overline{Ca} = \eta u_c/\gamma \epsilon^3$  and  $\overline{Ma} = \epsilon \gamma_T \Delta T/\eta u_c$ , where  $\eta$ ,  $\gamma$  and  $\gamma_T = |d\gamma/dT|$  denote the liquid film viscosity, surface tension and thermocapillary coefficient evaluated at  $T_{\text{hot}}$ , respectively. Further details about this model can be found in Refs. [11 and 12] where it is shown that  $\lambda_{\text{max}} = 2\pi h_o [4\gamma h_o/(3\kappa d_o \gamma_T \Delta T)]^{1/2} [(d_o/h_o) + \kappa - 1]$ . Eq. (1) contains a virtual singularity at  $\hat{H} = \hat{D}_v \equiv \hat{D}/(1 - \kappa)$  which, since  $\kappa < 1$ , is located in the unphysical domain beyond the top substrate, indicated by the dashed line in Fig. 3. This singularity reflects the plane where the surface shear diverges to infinity.

We now recast Eq.(1) into parameter free form

$$\frac{\partial H}{\partial T} + \nabla_{\parallel} \cdot \left[ H^3 \nabla_{\parallel}^3 H + \frac{H^2}{(1 - H)^2} \nabla_{\parallel} H \right] = 0 \quad (2)$$

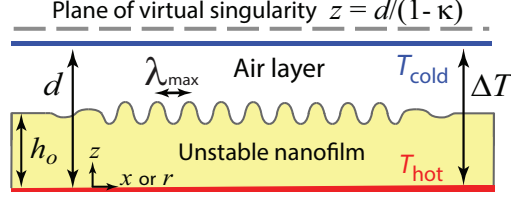


FIG. 3. (Color online) Geometry depicting linear instability of a slender liquid film driven by large thermocapillary forces induced by thermal conduction across a slender air gap.

by rescaling  $H = \hat{H}/H_c$  where  $H_c = \hat{D}/(1 - \kappa)$ ,  $\mathbf{X} = \hat{\mathbf{X}}/X_c$  (or  $\mathbf{R} = \hat{\mathbf{R}}/R_c$ ),  $T = \hat{T}/T_c$ ,  $X_c = (2\hat{D}\hat{D}_v/3\kappa\overline{Ma}\overline{Ca})^{1/2}$  and  $T_c = 4\hat{D}^2/(3\kappa^2\hat{D}_v\overline{Ma}^2\overline{Ca})$ . The lateral gradient  $\nabla_{\parallel}$  is similarly rescaled by  $X_c$ . The top substrate is then located at  $H = 1 - \kappa$  and the singularity at  $H = 1$ . We begin by proving that for  $H > 0$ , Eq. (2) admits no stable stationary states on a periodic or infinite domain by considering the Cahn-Hilliard (C-H) form [13],  $\partial H/\partial T = \nabla_{\parallel} \cdot [M(H)\nabla_{\parallel}(\delta\mathfrak{F}/\delta H)]$  where the Lyapunov free energy functional  $\mathfrak{F}$  is given by

$$\mathfrak{F}[H] = \int_{\Omega} \left( \frac{1}{2} |\nabla_{\parallel} H|^2 + U(H) \right) d\Omega, \quad (3)$$

the mobility coefficient  $M(H) = H^3$ ,  $\delta\mathfrak{F}/\delta H = -\nabla_{\parallel}^2 H + dU/dH$ , and the driving potential  $U(H) = H \ln[(1 - H)/H]$ . In contrast to conventional C-H systems described by a double well potential, here  $U(H)$  exhibits no global minimum and diverges at  $H = 1$ , as does  $dU/dH$  and  $d^4U/dH^4$ , as shown in Fig. 4. For periodic domains  $\Omega$ , it can be shown that  $d\mathfrak{F}/dT \leq 0$ . (For infinite domains, the proof requires that the integrand in  $\mathfrak{F}[H]$  be augmented by  $U[H(\mathbf{X} \rightarrow \infty, T)]$ .) Stationary states  $H_s$  with constant volume  $V = \int_{\Omega} H(\mathbf{X}, T) d\Omega$  can be found by identifying the extrema of  $\mathfrak{F}[H, p]$  subject to constraint through a Lagrange multiplier  $p$ :

$$\mathfrak{F}[H, p] = \int_{\Omega} \left( \frac{|\nabla_{\parallel} H|^2}{2} + U(H) \right) d\Omega - p \left( \int_{\Omega} H d\Omega - V \right). \quad (4)$$

Stationary solutions must exhibit a vanishing first variation in the free energy  $\delta\mathfrak{F}|_{H_s} = 0$  for arbitrarily small perturbations  $\delta H$ , which leads to a relation for the effective interfacial pressure

$$p = \left[ -\nabla_{\parallel}^2 H + \frac{dU}{dH} \right]_{H=H_s}. \quad (5)$$

It has been shown that for a generalized class of thin films equations [14] which includes forms like Eq. (2), there exist perturbations to stationary states of the form  $H_s + \epsilon\delta H$  with

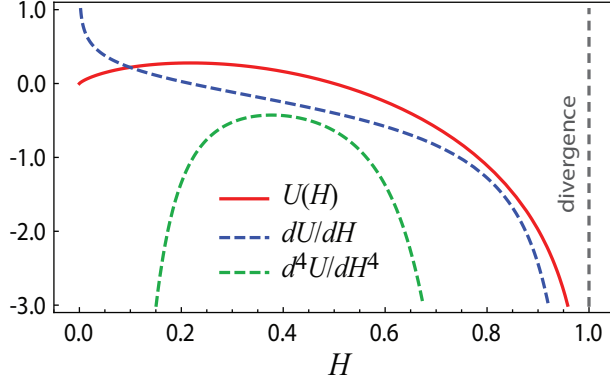


FIG. 4. (Color online) Plots of  $U(H)$ ,  $0.2dU/dH$  and  $0.005d^4U/dH^4$  for the thermocapillary equation. (Magnitudes were adjusted to accommodate the curves on a common scale.)

$\delta H \propto \partial^2 H_s / \partial X^2$  and  $\epsilon \ll 1$ , which lead to a negative second variation

$$\delta^2 \mathfrak{F}|_{H=H_s} = \int_{\Omega} \left( |\nabla_{\parallel} \delta H|^2 + \frac{d^2 U}{dH^2} \Big|_{H_s} \delta H^2 \right) d\Omega < 0 \quad (6)$$

whenever  $(d^4 U / dH^4)_{H \in H_s} < 0$ .

This implies there always exist nearby states with lower free energy. Since  $d^4 U / dH^4$  in Fig. 4 is everywhere negative, there are therefore no energetically stable stationary states for the thermocapillary system described by Eq. (2).

To gain further insight, we solved [15] Eq. (2) for planar and axisymmetric systems by splitting the form into two coupled second order equations. A mixed Lagrange finite element method was used and no flux conditions applied to the lateral domain sidewalls. The initial condition for planar flow was chosen to be  $H(X, 0) = (1 + 0.1 \cos K_{\max} X) / 3$  on the interval  $[0, \pi / K_{\max}]$  for  $K_{\max} = 2\pi / \lambda_{\max}$ . The computational domain contained about 20,000 elements ( $4 \times 10^{-8}$  minimum size) with quadratic shape functions to ensure sufficient resolution of the emerging cusp. The smallest mesh size  $\Delta \ll (\nabla_{\parallel}^2 H)^{-1}$  allowed this region to be tiled by at least ten elements. Time integration relied on a second order backward difference scheme with sufficiently small adaptive time steps enforced via tight tolerances. Evolution to cuspidal shapes required about 11,000 integration steps and were terminated when  $1 - H_{\text{apex}} < 2 \times 10^{-6}$ . Axisymmetric simulations were similarly treated. The numerical results shown in Fig. 5(a) reveal the (rapid) evolution of cuspidal shapes for planar (left) and axisymmetric (right) flow.

Fig. 5(b) reveals power law behavior indicative of self-similarity in the apical region where

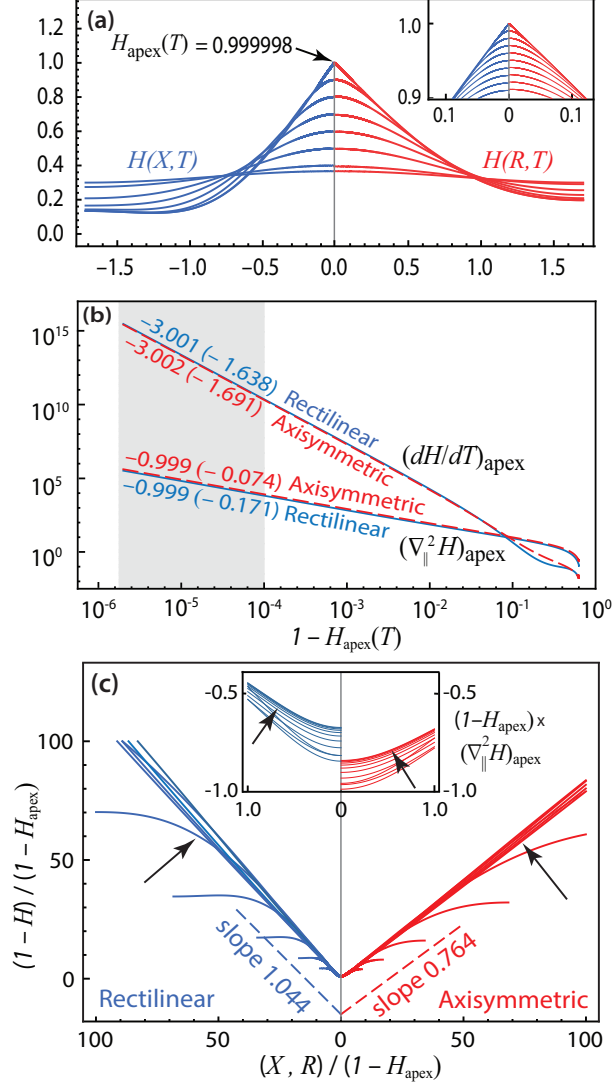


FIG. 5. (Color online) (a) Cusp interface shapes for  $H_{\text{apex}} = 0.367, 0.4, 0.5, \dots, 0.9, 0.999998$ . Inset: Magnified view for  $H_{\text{apex}} > 0.9$  in intervals of 0.01. (b) Log-log plots of  $dH/dT|_{\text{apex}}$  and  $\nabla_{\parallel}^2 H|_{\text{apex}}$  versus  $1 - H_{\text{apex}}$ . Slopes and intercept values (in parentheses) computed from least squared fits over shaded region. (c) Self-similar profiles of  $1 - H_{\text{apex}} = 0.2, 0.2/2, \dots, 0.2/2^{10}$ . Arrows indicate increasing time. Inset: Rescaled apical curvature.

$(dH/dT)_{\text{apex}} \sim (1 - H_{\text{apex}})^{-3}$  and  $(\nabla_{\parallel}^2 H)_{\text{apex}} \sim (1 - H_{\text{apex}})^{-1}$ . These exponents extend more than five decades in time and suggest two local scaling balances, namely  $(1 - H_{\text{apex}})/(T_c - T) \sim (1 - H_{\text{apex}})^{-3}$  and  $(1 - H_{\text{apex}})/X^2 \sim (1 - H_{\text{apex}})^{-1}$ , where  $T_c$  denotes the blowup time when  $H_{\text{apex}} = 1$ . These relations indicate  $X \sim T^{1/4} \sim (1 - H_{\text{apex}})$ . Although the model given by Eq. (2) is no longer valid beyond  $H = 1 - \kappa$ , the virtual cusp singularity at  $H = 1$

acts as an attractor to self-focus the fluid into a conical shape whose apical radius shrinks toward a point. These scalings are also evident from expansion of Eq. (2) about the singular value  $H = 1$ :

$$\frac{\partial H}{\partial T} + \nabla_{\parallel} \cdot \left[ \nabla_{\parallel} \nabla_{\parallel}^2 H + \frac{\nabla_{\parallel} H}{(1-H)^2} \right] + \mathcal{O}(1-H)^{-1} = 0 . \quad (7)$$

We examine 1D ( $X$ ) and 2D axisymmetric flow ( $R$ ) by introducing the self-similar variables

$$\tau = (T_c - T)^{\frac{1}{4}}, \quad \eta = \frac{(X, R)}{\tau}, \quad 1 - H = \sum_{n=1}^{\infty} \tau^n w_n(\eta) . \quad (8)$$

Were the original governing equation exactly scale invariant as in other thin film systems, the series expansion in Eq. (8) would terminate exactly with the  $n = 1$  term. The  $1 - H$  term in the denominator of Eq. (2) precludes such simplification. We propose the series expansions

$$\frac{\partial H}{\partial T} = \sum_{n=1}^{\infty} \tau^{n-4} \mathcal{T}_n(w_1, \dots, w_n) \quad (9)$$

$$\nabla_d \cdot (H^3 \nabla_d \nabla_d^2 H) = \sum_{n=1}^{\infty} \tau^{n-4} \mathcal{S}_n(w_1, \dots, w_n) \quad (10)$$

$$\nabla_d \cdot \left[ \frac{H^2 \nabla_d H}{(1-H)^2} \right] = \sum_{n=1}^{\infty} \tau^{n-4} \mathcal{M}_n(w_1, \dots, w_n) , \quad (11)$$

where  $\nabla_d \equiv \hat{\mathbf{e}}_X \partial / \partial X$  or  $\hat{\mathbf{e}}_R \partial / \partial R$  and  $\hat{\mathbf{e}}_i$  denote unit vectors. To leading order  $n = 1$ , Eq. (2) reduces to the nonlinear, fourth order form

$$\mathcal{T}_1(w_1) + \mathcal{S}_1(w_1) + \mathcal{M}_1(w_1) = 0 , \quad (12)$$

$$\mathcal{T}_1(w_1) = \frac{1}{4} \left( w_1 - \eta \frac{dw_1}{d\eta} \right) \quad (13)$$

$$\mathcal{S}_1(w_1) = -\nabla_{\eta}^4 w_1 \quad \text{and} \quad \mathcal{M}_1(w_1) = \nabla_{\eta}^2 \left( \frac{1}{w_1} \right) . \quad (14)$$

where the operator subscripts denote differentiation with respect to  $\eta$ . (The  $n \geq 2$  equations containing  $w_1$  are linear.) Since solutions to Eq.(12) require symmetry about the origin,  $dw_1/d\eta|_{\eta=0} = 0$  and  $d^3 w_1/d\eta^3|_{\eta=0} = 0$ . For the boundary conditions as  $\eta \rightarrow \infty$ , we enforce the asymptotic behavior of the numerical solutions showing a stationary shape with fixed slope. The condition  $(\partial H / \partial T)|_{\eta \rightarrow \infty} \rightarrow 0$  yields the Robin condition  $\mathcal{T}_1(w_1)|_{\eta \rightarrow \infty} \rightarrow 0$ . To leading order, the asymptotic solution to Eq.(12) is satisfied by the Laurent series

$$w_1^{\infty} = \sum_{n=1}^{\infty} a_n \eta^{5-4n} = a_1 \eta + \mathcal{O}(\eta^{-3}) \quad \text{as } |\eta| \rightarrow \infty . \quad (15)$$

While the actual values of the asymptotic slope  $a_1 > 0$  must be computed numerically, the functional convergence to  $w_1^\infty$  can be seen by linearizing Eq. (12) such that  $w_1(\eta \rightarrow \infty) = w_1^\infty(\eta) + f(\eta)$ . This yields the non-homogeneous linear equation  $\mathcal{T}_1(f) + \mathcal{S}_1(f) - \nabla_\eta^2(f/(w_1^\infty)^2) = 0$  which in the limit  $|a_1| \ll 1$  leads to a singular perturbation problem with an inner boundary region influenced by the fourth order capillary term (not shown). We focus instead on global solutions of the linearized equation using a WKBJ approximation where  $f(\epsilon\eta) = \exp[\epsilon^{-4/3} \sum_{n=0}^{\infty} \epsilon^{4n/3} S_n(\epsilon\eta)]$  for  $\epsilon \ll 1$ . Matching terms of order  $\epsilon^{-4/3}$  and  $\epsilon^0$  and solving the resulting two ordinary equations yields the general solution

$$f \sim \beta_0 \eta + \sum_{n=1}^3 \frac{\beta_n}{\eta^\gamma} \exp\left[-\frac{3}{4^{4/3}} e^{\frac{2\pi i}{3} n} \eta^{\frac{4}{3}}\right] + \dots \quad (16)$$

with  $\gamma = 1$  and  $5/3$  for the rectilinear or axisymmetric case, respectively. Since the first two terms in the summation undergo diverging oscillatory behavior,  $\beta_1 = \beta_2$  must vanish. The two non-vanishing terms preceded by  $\beta_0$  and  $\beta_3$  reflect an infinitesimal shift to the far field slope and a rapidly decaying function. Were the analytic solution to Eq. (12) known in the vicinity of the origin, the coefficients  $\beta_0$  and  $\beta_3$  would be obtained by asymptotic matching. Absent that approach, the solutions to Eq. (12) are still constrained by the symmetry condition at the origin, which yields solutions only for discrete values of the far field slope, as computed next.

The numerical solutions [15] to Eq.(12) were computed on a finite domain  $0 \leq \eta \leq L$  subject to the boundary conditions described at  $\eta = 0$  (symmetry) and  $L$  (Robin). Mesh refinement and finite size studies were conducted to assure convergent solutions. Shown in Fig. 6 are the first six similarity solutions with key limiting values listed in Table I. The asymptotic slopes for the rectilinear solutions are larger than those for the axisymmetric ones and tend to cause stronger oscillations in the near field, which for axisymmetric geometry are relatively suppressed by the additional capillary pressure gradient stemming from the radial curvature.

Next we compare the values of the linear fitting coefficients obtained from the self-similar analysis leading to Eq.(12) with those values obtained from direct simulations of Eq. (2) shown in Fig. 5. It can be shown that to leading order  $w_1$ , the linear intercept value for  $dH_{\text{apex}}/dT$  is  $\log_{10} \left[ (w_1^{(p)}(0))^4 / 4 \right]$  and for  $(\nabla_{\parallel}^2 H)_{\text{apex}}$  is  $\log_{10} \left[ w_1^{(p)}(0) \nabla_{\parallel}^2 w_1^{(p)}(0) \right]$  where  $1 - H_{\text{apex}} \approx \tau w_1^{(p)}(0)$ . Substitution of the  $p = 1$  values in Table I into these relations yields intercept values for  $dH_{\text{apex}}/dT$  equal to -1.632 for the rectilinear case and -1.681 for the

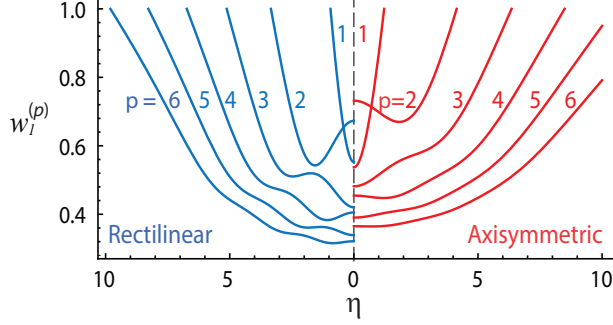


FIG. 6. (Color online) Leading order self-similar solutions  $w_1^{(p)}$  to Eq.(12). Only first six convergent solutions shown.

axisymmetric case. The corresponding values for  $(\nabla_{\parallel}^2 H)_{\text{apex}}$  are -0.175 and -0.078. These values are in excellent agreement with the intercept values shown in Fig. 5(b). Likewise, the slope values  $\lim_{\eta \rightarrow \infty} dw_1^{(1)}/d\eta$  for the leading solutions in Table I show excellent agreement when superposed on the collapsed profiles shown in Fig. 5(c). When converted to dimensional form, the asymptotic slope of the virtual cuspidal shape is given by the relation  $\lim_{\eta \rightarrow \infty} dw_1^{(1)}/d\eta \times (\gamma_T \Delta T / \gamma)^{1/2} [3\kappa/2(1 - \kappa)]^{1/2}$ . We next show that the mode  $w_1^{(1)}$  is

TABLE I. Computed values of the asymptotic interface slope, amplitude and curvature at the origin for the first  $p = 1 - 6$  similarity solutions to Eq.(12) to leading order  $w_1$  for rectilinear (blue) and axisymmetric (red) geometry.

$p$	$\lim_{\eta \rightarrow \infty} dw_1^{(p)}/d\eta$		$w_1^{(p)}(0)$		$\nabla_{\eta}^2 w_1^{(p)}(0)$	
1	1.0437	0.7639	0.5526	0.5372	1.2082	1.5563
2	0.3430	0.2474	0.6728	0.7317	-0.2316	-0.1624
3	0.2145	0.1610	0.4204	0.4816	0.2021	0.1669
4	0.1580	0.1196	0.4052	0.4544	-0.0884	-0.0438
5	0.1257	0.0962	0.3390	0.3902	0.0792	0.0526
6	0.1046	0.0806	0.3211	0.3649	-0.0364	-0.0087

self-selected over all other modes  $w_1^{(p \geq 2)}$ . Linear stability analysis of Eq. (7) is non-trivial since the self-similar base states evolve on multiple time scales  $\{\tau^n\}_{n=1}^{\infty}$ . However, since the late stage dynamics of Eq. (8) is dominated by  $w_1^{(p)}$ , it suffices to consider infinitesimal

perturbations which scale as  $w_1^{(p)}$ :

$$1 - H = \tau w_1^{(p)}(\eta) + \epsilon \tau^{1-4\lambda} \sum_{m=0}^{\infty} e^{im\theta} \phi_m(\eta) \quad (17)$$

where  $\theta$  denotes the polar coordinate in cylindrical geometry and  $\phi_m(\eta)$  the corresponding perturbation. The corresponding eigenvalue equation is given by

$$\mathcal{T}_1(\phi_m) + \mathcal{S}_1(\phi_m) + \delta\mathcal{M}_1(\phi_m) = \lambda\phi_m, \quad (18)$$

with  $\delta\mathcal{M}_1 = -\nabla_{\parallel}^2[\phi_m/(w_1^{(p)})^2]$ . (Note that the gradients in Eq. (12) must now include the  $\theta$  terms.) For localized perturbations that preserve constant slope in the far field,  $\mathcal{T}_1(\phi_m) = \lambda\phi_m$  as  $\eta \rightarrow \infty$ . Furthermore, since Eq. (7) is both space and time translationally invariant, there exist two trivial solutions as well, namely  $\cos\theta \times dw_1^{(p)}/d\eta$  with eigenvalue  $1/4$ , and  $(w_1^{(p)} - \eta dw_1^{(p)}/d\eta)/4$  with eigenvalue  $1$ . The eigenvalue spectrum for the first  $p = 1 - 6$  self-similar base states of Eq. (12) is plotted in Fig. 7. There are  $2p$  eigenvalues for each solution  $w_1^{(p)}$ ; however, the fundamental solution  $w_1^{(1)}$  is the only solution with no positive eigenvalues aside from those two reflecting time and space invariance. The cusp formation process is therefore dominated by self-selection of the  $w_1^{(1)}$  state.

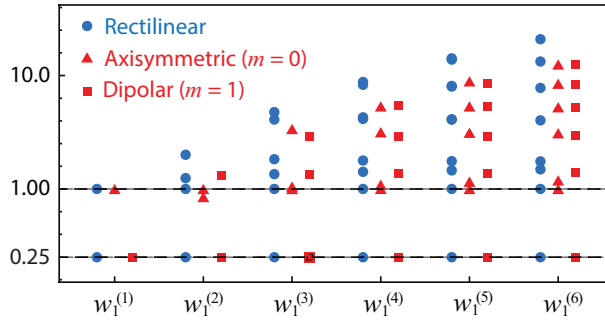


FIG. 7. Eigenvalue spectrum for Eq. (18) for perturbations to the first  $p = 1 - 6$  self-similar base states of Eq. (12) for rectilinear, axisymmetric and dipolar type modes.

In conclusion, we have identified a thin film system driven by surface shear where conical formations evolve by a self-reinforcing, self-similar mechanism. Rounded protrusions get rapidly drawn toward a virtual attractor resembling a line or point cusp. Aside from fundamental importance, this dynamical system offers a novel method for fabrication of unusual microarrays, whose shapes are much more difficult, costly and even impossible to manufacture by any other lithographic technique.

---

\* Corresponding author: stroian@caltech.edu

- [1] J. Eggers and M. A. Fontelos, *Singularities: Formation, Structure and Propagation* (Cambridge Univ. Press, 2015).
- [2] W. W. Zhang and J. R. Lister, *Phys. Fluids* **11**, 2454 (1999).
- [3] S. S. Thete, C. Anthony, O. A. Basaran, and P. Doshi, *Phys. Rev. E* **92**, 023014 (2015).
- [4] A. J. Bernoff, A. L. Bertozzi, and T. P. Witelski, *J. Stat. Phys.* **93**, 725 (1998).
- [5] R. Krechetnikov, *Phys. Fluids* **24**, 022111 (2012).
- [6] R. Krechetnikov, *Phys. Rev. E* **91**, 043019 (2015).
- [7] T. P. Witelski and A. J. Bernoff, *Physica D: Nonlin. Phen.* **147**, 155 (2000).
- [8] A. del Campo and E. Arzt, *Chem. Rev* **108**, 911 (2008).
- [9] E. McLeod, Y. Liu, and S. M. Troian, *Phys. Rev. Lett.* **106**, 175501 (2011).
- [10] K. M. Wisdom, J. A. Watson, X. Qua, F. Liua, G. S. Watson, and C. H. Chen, *PNAS* **110**, 7992 (2013).
- [11] M. Dietzel and S. M. Troian, *Phys. Rev. Lett.* **103**, 074501 (2009).
- [12] M. Dietzel and S. M. Troian, *J. Appl. Phys.* **108**, 074308 (2010).
- [13] V. S. Mitlin, *J. Colloid Interface Sci.* **156**, 491 (1993).
- [14] R. S. Laugesen and M. C. Pugh, *J. Diff. Eqns.* **182**, 377 (2002).
- [15] COMSOL Inc., Multiphysics V5.3, Burlington, MA, USA.